Synthesis and study of impendence spectroscopy properties of La0.6Ca0.2Na0.2MnO3 manganite perovskite prepared using sol–gel method

Faisal Alresheedi, Sobhi Hcini, Mohamed Lamjed Bouazizi, Michel Boudard, Abdessalem Dhahri

▶ **To cite this version:**

Faisal Alresheedi, Sobhi Hcini, Mohamed Lamjed Bouazizi, Michel Boudard, Abdessalem Dhahri. Synthesis and study of impendence spectroscopy properties of La0.6Ca0.2Na0.2MnO3 manganite perovskite prepared using sol–gel method. Journal of Materials Science: Materials in Electronics, 2020, 31 (11), pp.8248-8257. 10.1007/s10854-020-03360-4 . hal-03127764

HAL Id: hal-03127764

https://hal.univ-grenoble-alpes.fr/hal-03127764v1

Submitted on 11 Oct 2021

HAL is a multi-disciplinary open access archive for the deposit and dissemination of scientific research documents, whether they are published or not. The documents may come from teaching and research institutions in France or abroad, or from public or private research centers.

L'archive ouverte pluridisciplinaire **HAL**, est destinée au dépôt et à la diffusion de documents scientifiques de niveau recherche, publiés ou non, émanant des établissements d'enseignement et de recherche français ou étrangers, des laboratoires publics ou privés.

Synthesis and study of impendence spectroscopy properties of $La_{0.6}Ca_{0.2}Na_{0.2}MnO_3$ manganite perovskite prepared using sol-gel method

Faisal Alresheedi [1], Sobhi Hcini [2,*], Mohamed Lamjed Bouazizi [3], Michel Boudard [4], Abdessalem Dhahri [5]

[1] Department of Physics, College of Science, Qassim University, Buraidah-51452, Saudi Arabia.
[2] Research unit of valorization and optimization of exploitation of resources, Faculty of Science and Technology of Sidi Bouzid, University Campus Agricultural City, University of Kairouan, 9100 Sidi Bouzid, Tunisia.
[3] Department of Mechanical Engineering, College of Engineering, Prince Sattam Bin Abdulaziz University, 11942 Alkharj, Saudi Arabia.
[4] LMGP, University of Grenoble Alpes, CNRS, 38000 Grenoble, France.
[5] Laboratory of Physical Chemistry of Materials, Faculty of Science of Monastir, Department of Physics, 5019, University of Monastir, Monastir, Tunisia.

* Corresponding authors. *E-mail address:* hcini.s@yahoo.com, hcini.fstsb@gmail.com (S. Hcini)

Abstract

$La_{0.6}Ca_{0.2}Na_{0.2}MnO_3$ manganite was prepared using sol-gel method. Rietveld refinement of XRD pattern indicates that the prepared sample crystallizes in the rhombohedral $R\bar{3}c$ structure. The impendence spectroscopy properties of the sample were studied by performing a series of measurements as a function of temperature and frequency of conductivity, dielectric constants, modulus and impedance. From these measurements, the metal-semiconductor behaviour was observed for the sample at a transition temperature of the order of 240 K. The studies of imaginary part of permittivity and tangent loss reveal that the prepared material may be a good candidate for low-frequency energy storage devices. An electrical relaxation phenomenon with non-Debye nature was observed in variations of imaginary parts of modulus and impedance. Electrical parameters deduced from the Nyquist plots analyses using an equivalent circuit reveal that the conduction process for the sample was caused due to the grain boundaries contribution.

Keywords: Manganites; Sol–gel method; Microstructural analysis; Conductivity; Dielectric constants; Modulus; Nyquist plots.

1. Introduction

Perovskite-type manganese oxides are complex materials because of their extremely high chemical stability over a wide range of compositions which leads to numerous modifications in their properties. They have been widely studied in recent years to find out more and understand the different possible interactions within this structure rendered complex by the mixed valence of manganese (Mn^{3+}/Mn^{4+}). In particular, the study of manganese perovskites experienced a renewed interest with the discovery of what is called colossal magnetoresistance [1]. This property entails of a radical change in electrical resistivity when a magnetic field is applied to these materials. This feature makes them interesting for applications such as new read heads in order to increase the memory capacity of hard drives.

The manganites with perovskite structure adopt $Ln_{1-x}M_xMnO_3$ as general formula where Ln is a trivalent rare earth element (La^{3+}, Pr^{3+}, Nd^{3+}, etc…) and M is a divalent alkaline earth metal (Ca^{2+}, Ba^{2+}, Sr^{2+}, etc…). The first studies of these manganites were conducted in the $La_{1-x}(Ca/Sr/Ba)_xMnO_3$ systems [2-4]. It was demonstrated that by substituting lanthanum with a divalent cation, it was possible to alter the physical properties of these materials. Indeed, depending on the rate of substitution, these materials can act as insulators, semiconductors or even metals. Moreover, depending on the degree of substitution, they can be either ferromagnetic or antiferromagnetic. Since then, the same richness of physical properties of the manganite perovskites has been found in other systems (see [5] for a review and references therein).

One of the fundamental characteristics of manganite perovskites is the strong correlations between their microstructural and physical properties. This correlation has been interpreted based on the double exchange (DE) mechanism [6]. However, the DE is not sufficient to explain all the properties of manganites. Several other parameters can be considered in order to fully explain their properties, in particular the density of the carriers

(i.e. the Mn^{3+}/Mn^{4+} ratio), the average radius of A and B sites and the disorder caused by the size difference of the cations on A site (mismatch effect).

This work is concerned with the family of lanthanum manganites and its calcium-doped alloys, $La_{1-x}Ca_xMnO_3$, a subject of considerable renewed interest after the discovery of CMR in La-Ca-Mn-O system and its related films [7, 8]. In addition to the CMR effects, unusual magnetic and electrical properties of lanthanum manganites are also well known. For example, for a broad doping domain in $La_{1-x}Ca_xMnO_3$ system ($0.2 \leq x < 0.5$), an insulator-metallic transition (IM) is associated with a paramagnetic (PM)-ferromagnetic (FM) transition, which is traditionally explained by the DE mechanism [9]. The different compositions of $La_{1-x}Ca_xMnO_3$ have been widely treated [10-16]. However, studies related to this system have been continued and several substitutions have been made to enhance its properties both at the fundamental scale and for potential applications [17-23].

Considering that $La_{1-x}Ca_xMnO_3$ manganites are well studied in the literature and their properties are well explicated with different substitutions, we chose to study in this work a combined compound belonging to this family with monovalent ion substitution. Using the sol-gel method, we prepared a perovskite oxide with $La_{0.6}Ca_{0.2}Na_{0.2}MnO_3$ composition and investigated its microstructural and impendence spectroscopy (IS) properties.

2. Experimental

2.1. Synthesis

Sol-gel method was used to synthesize $La_{0.6}Ca_{0.2}Na_{0.2}MnO_3$ perovskite as shown in Fig. 1. The stoichiometric amounts of lanthanum, calcium, sodium and manganese nitrates with high purity were taken in the required molar weight ratio to meet the molecular formula of the $La_{0.6}Ca_{0.2}Na_{0.2}MnO_3$ sample. The nitrates were dissolved in distilled water with thermal stirring at 90 °C, followed by the addition of citric acid which is used as complexation agent for the different metal cations. Subsequently, we have adjusted the pH of the solution to

around 7 by adding the ammonia. After this step, we added the ethylene glycol which has been used as a polymerization agent. After approximately 4 h, the formation of a viscous liquid (gel) is observed, which was subsequently dried in an oven at 200 °C (for 6 h). The resulting precursor was ground and the obtained powder was undergone a few cycles of grinding, pelleting and sintering. Finally, the structure of $La_{0.7}Ba_{0.15}Sr_{0.15}CoO_3$ sample was well formed at 1100 °C (for 24 h).

2.2. Measurements

XRD pattern was registered using "Panalytical X'Pert Pro System" two-circle automatic diffractometer operating at copper wavelength (λ=1.5406 Å) with a filter of Nickel to eliminate the K_β ray. The measurement was made in Bragg Brentano geometry in a divergent beam, with 0.017 ° step and 18 s counting time per step in an angular range of $10 \leq 2\theta \leq 100°$. Rietveld method using FullProf software was used for structural analysis [24]. The morphology of the sample was examined in pellet form by Scanning Electron Microscopy (SEM) using a Philips XL 30 microscope equipped with an electron gun, with 15 kV accelerating voltage. Electrical characterizations were made on the sample having a disk shape with a diameter of 10 mm and a thickness of approximately 2 mm using N4L-NumetriQ (model PSM1735) analyzer at different temperatures over the frequency range of 100 Hz – 5 MHz.

3. Results and discussions

3.1. Structural and morphological analyses

The obtained XRD diffractogram for $La_{0.6}Ca_{0.2}Na_{0.2}MnO_3$ perovskite is shown in Fig. 2a. The compound is crystallized well, and the majority phase was a perovskite whose diffraction peaks were indexed in the $R\bar{3}c$ rhombohedral symmetry. The structural refinement for the sample is shown in Fig. 2b. The refined cell parameters were a= b= 5.4859 (1) Å, c= 13.3963 (2), α = 90 °, β = 90 ° and γ = 120 °. The volume of the unit cell was V= 349.15 (1)

Å^3. The reliability factors obtained from the Rietveld refinement are the profile factor R_p(%) = 5.91, the weighted profile factor R_{wp}(%) = 8.48, the structure factor R_F(%)= 3.52, and the goodness of fit χ^2 (%)= 3.44 corresponded well with the literature. The average grains size was estimated from the XRD peaks using the following Scherer formula [25]:

$$D_{XRD} = \frac{0.9\,\lambda}{\beta\cos(\theta)} \quad (1)$$

where λ is the X-ray wavelength , β is the corrected full-width half maxima of the XRD peaks and θ is the Bragg angle. The estimated average size of grains was about 48 nm. For comparison, the obtained values of cell parameters for $La_{0.6}Ca_{0.2}Na_{0.2}MnO_3$ sample are smaller compared to those found for the undoped compound $La_{0.8}Ca_{0.2}MnO_3$ [26]. Obviously the Na-substitution of La causes the decrease of lattice parameters in $La_{0.8}Ca_{0.2}MnO_3$ sample, in agreement with the results found for $La_{1-x}Na_xMnO_3$ [27, 28]. The SEM image given in Fig. 2c shows a homogeneous morphology without any chemical contrast between the crystalline grains. This confirms that no secondary phase was observed outside the perovskite phase of $La_{0.6}Ca_{0.2}Na_{0.2}MnO_3$ compound. This micrograph also reveals that the sample consists of small particles with average size D_{MEB}= 1.75 μm (Fig. 2d), significantly larger than the value determined from XRD pattern. Certainly, each particle analyzed by SEM is constituted by a multitude of much smaller grains, and as the X-rays have a much higher resolution than that of the SEM, the grains size estimated from XRD is much smaller than that obtained from SEM [29].

3.2. Electrical conductivity study

In general, the electrical conductivity (σ) of $(Ln^{3+}_{1-x}M^{2+}_x)(Mn^{3+}_{1-x}Mn^{4+}_x)O^{2-}_3$ manganite systems is mainly caused by the electron hopping between Mn^{3+} and Mn^{4+} neighboring ions through the oxygen anion O^{2-} [30]. In order to analyze the hopping conduction mechanism of the prepared $(Ln^{3+}_{0.6}Ca^{2+}_{0.2}Na^{+}_{0.2})(Mn^{3+}_{0.4}Mn^{4+}_{0.6})O^{2-}_3$ sample, the variation of its conductivity is

presented in Fig. 3 with frequency and temperature. The σ values were calculated using the following relation [31]:

$$\sigma = G\frac{t}{A} \quad (2)$$

where G is the electrical conductance, t is the thickness of the pellet and A is the area of cross section of the pellet. From Fig. 3, it can be seen that the $\sigma(f)$ curves present similar variations for the different temperatures. In fact, the conductivity values remain practically constant in the low frequency region up to a frequency value $f_h \leq 10^5$ Hz which is known as hopping frequency. This constancy could be explained by the fact that the electron hopping between Mn^{3+} - Mn^{4+} ions is low due to the higher activity of weakly conductive grain boundaries in this frequency region. This low frequencies conductivity corresponds to the *dc* conductivity (σ_{dc}). Subsequently, an exponential increase in the conductivity was observed above f_h. This behavior is caused as conductive grains become more active in this frequency range, which increases the electron hopping between Mn^{3+} - Mn^{4+} ions and consequently promotes the conduction process in the sample. This high frequency conductivity corresponds to the *ac* conductivity (σ_{ac}). To modelize σ-values, we used the following mathematical relation (Jonscher power law) [32]:

$$\sigma_{tot} = \sigma_{dc} + A\omega^s \quad (3)$$

where, σ_{dc} is the *dc* conductivity, A and s are the pre-exponential and exponent factors, respectively. Fig. 3 shows much affinity between theoretical and experimental values. The adjustment values of σ_{dc} and s are plotted in Fig.4a. This figure proves that the sample experienced a metal–semiconductor (MS) transition at T_{MS} = 240 K. Similar transitions from the conductivity curves were observed in other works [33-37]. In addition, all the s-values are greater than unity. According to the Funke criterion [38], this means that the electrons hopping between Mn^{3+} - Mn^{4+} ions happens between neighboring sites. At a high temperature

range, the *dc* conductivity behavior is well fitted by the following mathematical formula so called Arrhenius relation [39]:

$$\sigma_{dc} = \sigma_0 exp\left(-\frac{E_{dc}}{k_B T}\right) \quad (4)$$

where σ_0 = pre-exponential factor and k_B= Boltzmann constant. Eq. (4) is being used to calculate the activation energy (E_{dc}) required in the sample by plotting the graph of Ln(σ_{dc}) vs. $(1000/T)$ in Fig.4b. The E_{dc} value expected from the slope of the plot is 0.298 eV, which is smaller than those for other materials [40-42], suggesting that the present sample is a good conductor.

3.3. Dielectric study

Fig. 5a presents the variation of imaginary part of permittivity (ε'') with frequency and temperature. The values of ε'' were calculated from the conductivity data using the following relation [31]:

$$\varepsilon'' = \frac{\sigma}{\omega \varepsilon_0} \quad (5)$$

where $\omega = 2\pi f$ is the angular frequency and ε_0= 8.854×10^{-12} F/m is the permittivity of free space. The imaginary part of permittivity (ε'') of a sample provides a storage energy when a suitable electrical potential is applied to the sample. This dielectric constant depends on two factors, namely the polarization vector and the capacitance. From Fig. 5a, it can be observed that, in the low frequency range, the values of ε'' are high and they prove the MS transition observed for the sample at 240 K. The higher ε''-values at low frequencies reveal that the prepared material may be a good candidate for low frequency energy storage devices of the applied alternating electric field. Similarly, at higher frequencies, the ε''-values decrease, increasing the energy storage capacity. Fig. 5b represents the variation of loss factor ($tan\delta$) with frequency. The dielectric loss factor ($tan\delta$) for the sample was calculated using this relation [32]:

$$\tan(\delta) = \frac{\varepsilon''}{\varepsilon'} \quad (6)$$

where ε'' and ε' are the imaginary and the real parts of permittivity, respectively. The values of *tanδ* of a material give an idea of the electrical energy loss due to dielectric relaxation, dielectric resonance, conduction, and from non-linear processes [43]. The preliminary development of the dielectric loss in a material may be caused by a mismatch between the frequency of the applied electric field with the electric displacement vectors. There are two types of dielectric loss observed in materials: one resulting from the crystalline symmetry, the applied alternating electric field frequency and the temperature, which is called intrinsic loss, while the combing effect of impurities, structural defects, grain boundaries, micro-cracks, dislocations, and vacancies is called extrinsic loss. For the present sample, in the lowest frequency range, the values of loss factor are high (Fig. 5b), but in the higher frequency range, the loss factor decreases. Thus, the prepared sample is a potential material for the manufacture of energy storage devices. In terms of application, this material can be used in energy storage capacitors, sensors, actuators and resonant wave devices.

3.4. Electrical modulus analysis

The real (*M′*) and imaginary (*M″*) parts of electrical modulus for $La_{0.6}Ca_{0.2}Na_{0.2}MnO_3$ perovskite were given from the real (ε') and the imaginary (ε'') parts of permittivity using the two following equations [32]:

$$M' = \frac{\varepsilon'}{(\varepsilon'^2 + \varepsilon''^2)} \quad (7)$$

$$M'' = \frac{\varepsilon''}{(\varepsilon'^2 + \varepsilon''^2)} \quad (8)$$

Fig. 6a indicates the behaviours of real part of modulus (*M′*) against frequency and temperature. In the low frequency region, it is observed that *M′* values are very small. This confirms that the electrode polarization makes a negligible contribution in the material [44]. As the frequency increases, the *M′* values continue to increase with saturation tending up to reach a maximum asymptotic value. This may be due to the short-range mobility of charges

carriers [45, 46]. Fig. 6b indicates the behaviour of the imaginary component of modulus. It can be observed that *M''* has a similar profile for each temperature. In fact, in the beginning, the *M''* increases with increasing frequency until it attains optimal value at ($f_{M''}^{max}$). Then, with increasing frequency, the *M''(f)* values decrease. The *M''(f)* values were well fitted using the Kohlrausch, Williams and Watts (KWW) function [47]:

$$M'' = M''_{max} / \left[1 - \beta + \left(\frac{\beta}{1+\beta}\right)\left(\beta\left(\frac{f_{max}}{f}\right) + \left(\frac{f}{f_{max}}\right)^{\beta}\right)\right] \quad (9)$$

where M''_{max} is the peak maxima and f_{max} its corresponding frequency, and β is the stretching factor ($0 < \beta < 1$) [48]. In Table 1, the results of the fitting parameters using Eq. (9) have been summarized. Two important points can be taken into account from this table: the β-values are less than unity which demonstrates the non-Debye nature of the sample [48], and these values prove the presence of MS transition observed for the sample at 240 K. In Table 1 we have grouped the values of the relaxation frequency (f_{max}) that allow us to calculate the relaxation time ($\tau_{M''}$) through this equation:

$$\tau_{M''} = 1/2\pi f_{max}, \quad (10)$$

Fig. 7 shows the reverse temperature variation of the relaxation time ($\tau_{M''}$) for $La_{0.6}Ca_{0.2}Na_{0.2}MnO_3$ perovskite. The Arrhenius relation can be also used to modelize the temperature reliance of the relaxation time as [39]:

$$\tau_{M''} = \tau_o \, exp\left(\frac{E_{M''}}{k_B T}\right) \quad (11)$$

with τ_0 is the pre-exponential factor. The $E_{M''}$ value predictable from the linear fit of the curve is equal to 0.285 eV. This value corresponds well with the deduced one from the *dc* conductivity (E_{dc}), and this is an indication that the relaxation phenomenon, as well as the electrical conductivity, contribute to the same defect.

3.5. Impedance analysis

Fig. 8 (a) and (b) represent the variations of the real (Z') and imaginary (Z'') parts of impedance with a wide range of frequency and temperature. It is found that the values of Z' decrease with increasing frequency, thus resulting in an increase in the conductivity of the material. For high frequencies, the Z' values merge with each other, due to a possible release of the space charge [30] and the reduction of the barrier properties of the material, and this can be interpreted by the presence of a space charge polarization. This behavior is in agreement with the results reported in the literature for several materials [40-42, 49, 50]. The Z'' curves are characterized by the appearance of peaks that shift in agreement with the MS transition. This behaviour describes the type of dielectric relaxation phenomenon that takes place in the material, caused by the presence of almost immobile ions (Mn^{3+} and Mn^{4+} in our case) at low temperatures and defects and vacancies at high temperatures [30]. The Arrhenius relation can also be used to modelize the temperature variation of the relaxation time deduced from *Z''(f)* data. The estimated activation energy from $\mathrm{Ln}(\tau_{Z''})$ vs. *(1000/T)* plot (Fig. 9) is found as $E_{Z''}$= 0.294 eV. This value matches well will the deduced ones from the *dc* conductivity (E_{dc}) and relaxation time of modulus ($E_{M''}$). The plot of *Z''(f, T)* is presented in Fig. 10 in the scaled coordinates (*i.e.* Z''/Z''_{max} *vs.* $\log(f/f_{max})$). Fig. 10 shows that all normalized curves collapse into a single curve for all the temperature ranges which indicates that the relaxation time distribution is independent of temperature [42].

Fig. 11 displays the complex impedance curves (named Nyquist diagrams, i.e. Z″ vs. Z' plots) at different temperatures for $La_{0.6}Ca_{0.2}Na_{0.2}MnO_3$ perovskite. It is evident from Fig. 11 that for all the temperatures, the impedance spectra shows semicircle arcs. The semicircles are the result of the grain boundary conduction, meaning that the conduction process in the samples is principally related to the grain boundary contribution. To prove this observation, it is necessary to modelize the Nyquist diagrams. The suitable equivalent circuit configuration is

of the type (R_g + R_{gb}//CPE_{gb}) [51] (see Fig. 11). In this circuit, R_g and R_{gb} respectively designate the resistances of grain and grain boundary, and CPE_{gb} the grain boundary constant phase elements. The impedance response of a constant phase element (*CPE*) can be defined as [40]:

$$Z_{CPE} = \frac{1}{Q(j\omega)^{\alpha}} \tag{12}$$

here, Q and α are the *CPE* parameters which are frequency independent. The expressions of real (Z') and imaginary (Z'') components of impedance related to the equivalent circuit are given as [37]:

$$Z' = R_g + \frac{R_{gb}+(1+R_{gb}Q\omega^{\alpha}\cos(\frac{p\pi}{2}))}{(1+R_{gb}Q\omega^{\alpha}\cos(\frac{p\pi}{2}))^2 + (R_{gb}Q\omega^{\alpha}\sin(\frac{\alpha\pi}{2}))^2} \tag{13}$$

$$-Z'' = \frac{R_{gb}^2 Q\omega^{\alpha}\sin(\frac{\alpha\pi}{2}))}{(1+R_{gb}Q\omega^{\alpha}\cos(\frac{\alpha\pi}{2}))^2 + (R_p Q\omega^{\alpha}\sin(\frac{\alpha\pi}{2}))^2} \tag{14}$$

The modeling of impedance spectra was performed using *Zview* software [52]. A good agreement between the experimental spectra and the calculated ones was observed. The R_g, R_{gb}, CPE_{gb} and α parameters were evaluated for each temperature and have been listed in Table 2. In fact, the estimated R_{gb} values are more important than R_g values, as they confirm that the conduction process in the sample is basically related to the grain boundary apport as cited previously.

4. Conclusion

$La_{0.6}Ca_{0.2}Na_{0.2}MnO_3$ perovskite which crystallizes in the rhombohedral $R\bar{3}c$ structure was prepared using sol-gel technique. The impendence spectroscopy (IS) studies reveal that the sample presents a metal–semiconductor (MS) transition at T_{MS}= 240 K, and a relaxation phenomenon with non-Debye nature. Very close values of activation energies were deduced from relaxation time and dc-conductivity as E_{dc} = 0.298 eV, $E_{M''}$ = 0.285 eV and $E_{Z''}$= 0.294 eV. The equivalent electrical circuit (R_g+ R_{gb}//CPE_{gb}) is the best model for modeling the Nyquist data. In terms of application, the sample can be used in some interesting applications such as in energy storage capacitors, sensors, actuators and resonant wave devices.

Acknowledgements

This work was supported by the Deanship of Scientific Research at Prince Sattam Bin Abdulaziz University under the research Project Number 2017/01/7373.

References

[1] S. Hcini, S. Zemni, A. Triki, H. Rahmouni, M. Boudard, J. Alloys Compd. 509 (2011) 1394.

[2] G.H. Jonker, J.H. van Santen, Physica 16 (1950) 337.

[3] J.H. Van Santen, G.H. Jonker, Physica 16 (1950) 599.

[4] E.O. Wollan, W.C. Koehler, Phys. Rev. 100 (1955) 545.

[5] M.B. Salomon, M. Jaime, Rev. Mod. Phys. 73 (2001) 583.

[6] C. Zener, Phys. Rev. 81 (1951) 440.

[7] R. von Helmolt, J. Wecker, B. Holzapfel, L. Schultz, K. Samwer, Phys. Rev. Lett. 71, (1993) 2331.

[8] S. Jin, T.H. Tiefel, M. McCormack, R.A. Fastnacht, R. Ramesh, L.H. Chen, Science 264 (1994) 413.

[9] H.D. Zhou, R.K. Zheng, G. Li, S.J. Feng, F.Liu, X.J. Fan, X.G. Lia, Eur. Phys. J. B 26 (2002) 467.

[10] M. Pissas, G. Papavassiliou, J. Phys.: Condens. Matter 16 (2004) 6527.

[11] B.M. Nagabhushana, R.P. Sreekanth Chakradhar, K.P. Ramesh, C. Shivakumara, G.T. Chandrappa, Mater. Chem. Phys. 102 (2007) 47.

[12] R. Laiho, K.G. Lisunov, E. Lahderanta, V.N. Stamov, V.S. Zakhvalinskii, J. Phys.: Condens. Matter 13 (2001) 1233.

[13] A.E. Pantoja, H.J. Trodahl, R.G. Buckley, Y. Tomioka, Y. Tokura, J. Phys.: Condens. Matter 13 (2001) 3741.

[14] S.V. Trukhanov, N.V. Kasper, I.O. Troyanchuk, M. Tovar, H. Szymczak, K. Bärner, J. Solid State Chem. 169 (2002) 85.

[15] Q. Yang, J. Yao, K. Zhang, W. Wang, X. Zuo, H. Tang, M. Wu, G. Li, J. Electroanal. Chem. 833 (2019) 1.

[16] X.H. Huang, H.Y. Lin, Z.J. Cheng, Physica B: Condensed Matter, 529 (2018) 16.

[17] The-Long Phan, Y.D. Zhang, P. Zhang, T.D. Thanh, S.C. Yu, J. Appl. Phys. 112 (2012) 093906.

[18] P. Singh, V. Kumar, G.L. Bhalla, P.K. Siwach, O.N. Srivastava, N. Khare, Solid State Commun. 140 (2006) 395.

[19] R. Yadav, V. Shelke, J Mater Sci: Mater Electron 24 (2013) 1141.

[20] T.A. Ho, N.T. Dang, The-Long Phan, D.S. Yang, B.W. Lee, S.C. Yu, J. Alloys Compd. 676 (2016) 305.

[21] F. Ayadi, S. Ammar, W. Cheikhrouhou-Koubaa, A. Cheikhrouhou, T. Gaudisson, S. Reguer, S. Nowak, J.Monnier, L. Sicard, J. Alloys Compd. 691 (2017) 474.
[22] G. Dong, Y. Liu, S. Zhang, K. Chu, H. Li, X. Pu, T. Sun, F. Ji, X. Liu, Ceram. Int. 45 (2019) 21448.
[23] U. Chaudhuri, A. Chanda, R. Mahendiran, J. Magn. Magn. Mater. 499 (2020)166287.
[24] H.M. Rietveld, J. Appl. Cryst. 2 (1969) 65.
[25] R. Hamdi, A. Tozri, M. Smari, K. Nouri, E. Dhahri, L. Bessais, J. Mol. Struct. 1175 (2019) 844.
[26] S.O. Manjunatha, A. Rao, V.P.S. Awana, G.S. Okram, J. Magn. Magn. Mater. 394 (2015) 130.
[27] O.Z. Yanchevskii, A.I. Tovstolytkin, O.I. V'yunov, D.A. Durilin, A.G. Belous, Inorganic Materials 40 (2004) 744.
[28] N. Dodiya, D. Varshney, J. Mol. Struct. 1031 (2013) 104.
[29] E. Oumezzine, S. Hcini, E.K. Hlil, E. Dhahri, M. Oumezzine, J. Alloys Compd. 615 (2014) 553.
[30] S. Khadhraoui, A. Triki, S. Hcini, S. Zemni, M. Oumezzine, J. Magn. Magn. Mater. 371 (2014) 69.
[31] M. Hsini, N. Hamdaoui, S. Hcini, M.L. Bouazizi, S. Zemni, L. Beji, Phase Transitions 91 (2018) 316.
[32] S. Hcini, S. Khadhraoui, A. Triki, S. Zemni, M. Boudard and M. Oumezzine, J. Supercond. Nov. Magn. 27 (2014) 195.
[33] S. Hcini, E. Oumezzine, M. Baazaoui, H. Rahmouni, K. Khirouni, E. K. Hlil, M. Oumezzine, Appl. Phys. A. 120 (2015) 1453.
[34] A. Dhahri, Ja. Dhahri, S. Hcini, N. Talbi, E. K. Hlil, M. Oumezzine, K. Khirouni, Appl. Phys. A. 120 (2015) 247.
[35] H. Rahmouni, A. Dhahri, K. Khirouni, J. Alloys Compd. 591 (2014) 259.
[36] R. Bellouz, S. Kallel, K. Khirouni, O. Pena, M. Oumezzine, Ceram. Int. 41 (2015) 1929.
[37] M. Chebaane, N. Talbi, A. Dhahri, M. Oumezzine, K. Khirouni 426 (2017) 646.
[38] K. Funke, Prog. Solid State Chem. 22 (1993) 111.
[39] S. Hcini, A. Omri, M. Boudard, M.L. Bouazizi, A. Dhahri, K. Touileb. J Mater Sci: Mater. Electron. 29 (2018) 6879.
[40] D. Tlili, N. Hamdaoui, S. Hcini, M.L. Bouazizi, S. Zemni, Phase Transitions 90 (2017) 644.
[41] M.H. Dhaou, S. Hcini, A. Mallah, M.L. Bouazizi, A. Jemni, Appl. Phys. A. 8 (2017) 123.

[42] E. Oumezzine, S. Hcini, F.I.H. Rhouma, M. Oumezzine, J. Alloys Compd. 726 (2017) 187.
[43] L. Alexander, H. P. Klug, J. Appl. Phys. 21 (1950) 137.
[44] N.H. Vasoya, P.K. Jha, K.G. Saija, S.N. Dolia, K.B. Zankat, and K.B. Modi, J. Electron. Mater. 45 (2016) 917.
[45] S. Saha, T. P. Sinha, Phys. Rev. B 65 (2005) 1341.
[46] K.P. Padmasree, D.D. Kanchan, A.R. Kulkami, Solid State Ionics 177 (2006) 475.
[47] R. Bergman, J. Appl. Phys. 88 (2000) 1356.
[48] K.S. Rao, P.M. Krishna, D.M. Prasad, D. Gangadharudu, J. Mater. Sci. 42 (2007) 4801.
[49] F.B. Abdallah, A. Benali, S. Azizi, M. Triki, E. Dhahri, M.P.F. Graça, M.A. Valente, J. Mater. Sci.: Mater. Electron. 30 (2019) 8457.
[50] F.B. Abdallah, A. Benali, M. Triki, E. Dhahri, M.P.F. Graça, M.A. Valente, Superlattice Microst. 117 (2018) 260.
[51] S. Khadhraoui, A. Triki, S. Hcini, S. Zemni, M. Oumezzine, J. Alloys Compd. 574 (2013) 290.
[52] Johnson D. ZView: a software program for IES analysis. Version 2.8. Southern Pines, NC: Scribner Associates, Inc.; 2008.

Figure captions

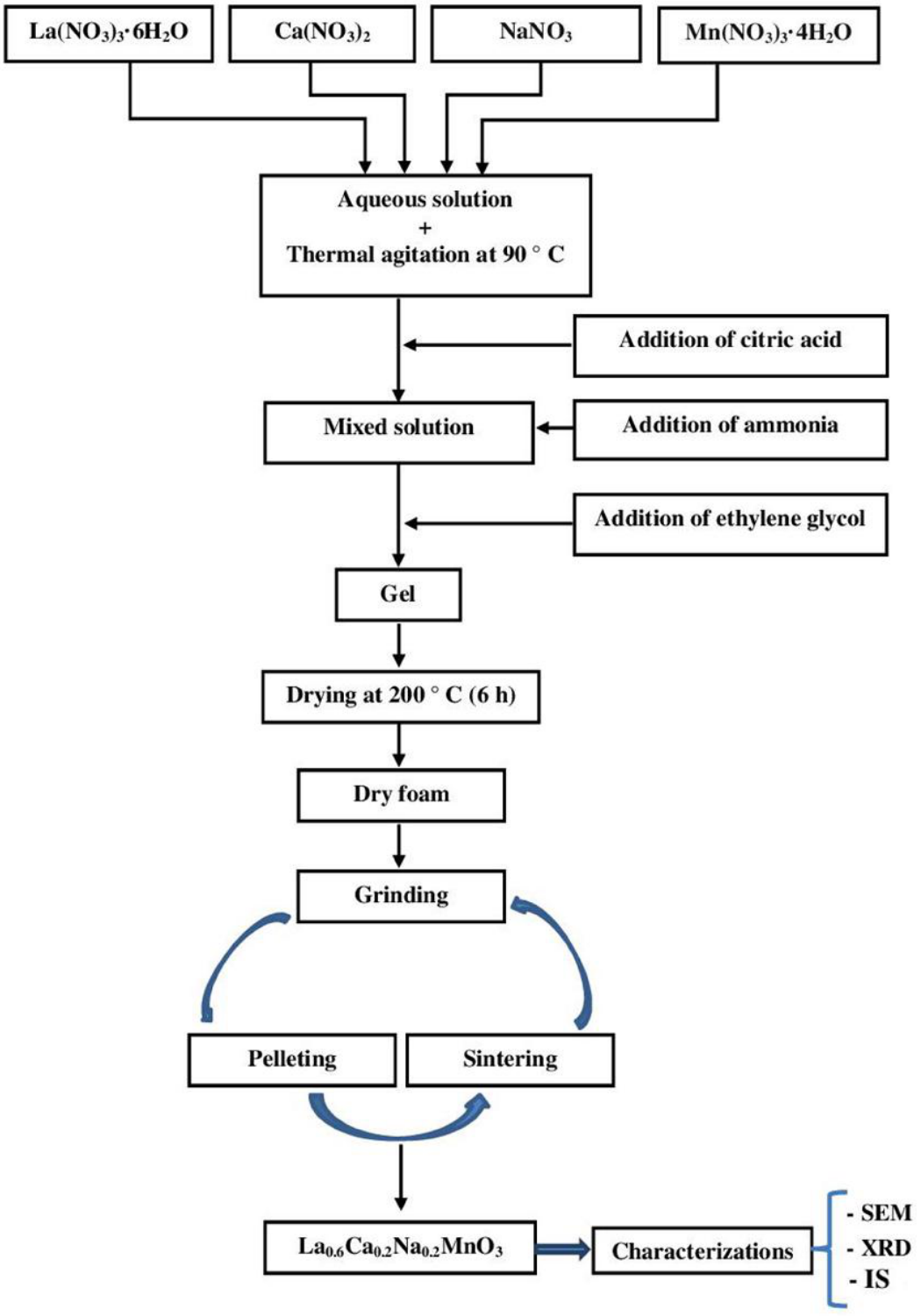

Fig. 1: Synthesis steps of $La_{0.6}Ca_{0.2}Na_{0.2}MnO_3$ perovskite using sol-gel method. SEM, XRD and IS abbreviations designate scanning electron microscope, X-rays diffraction and impedance spectroscopy, respectively.

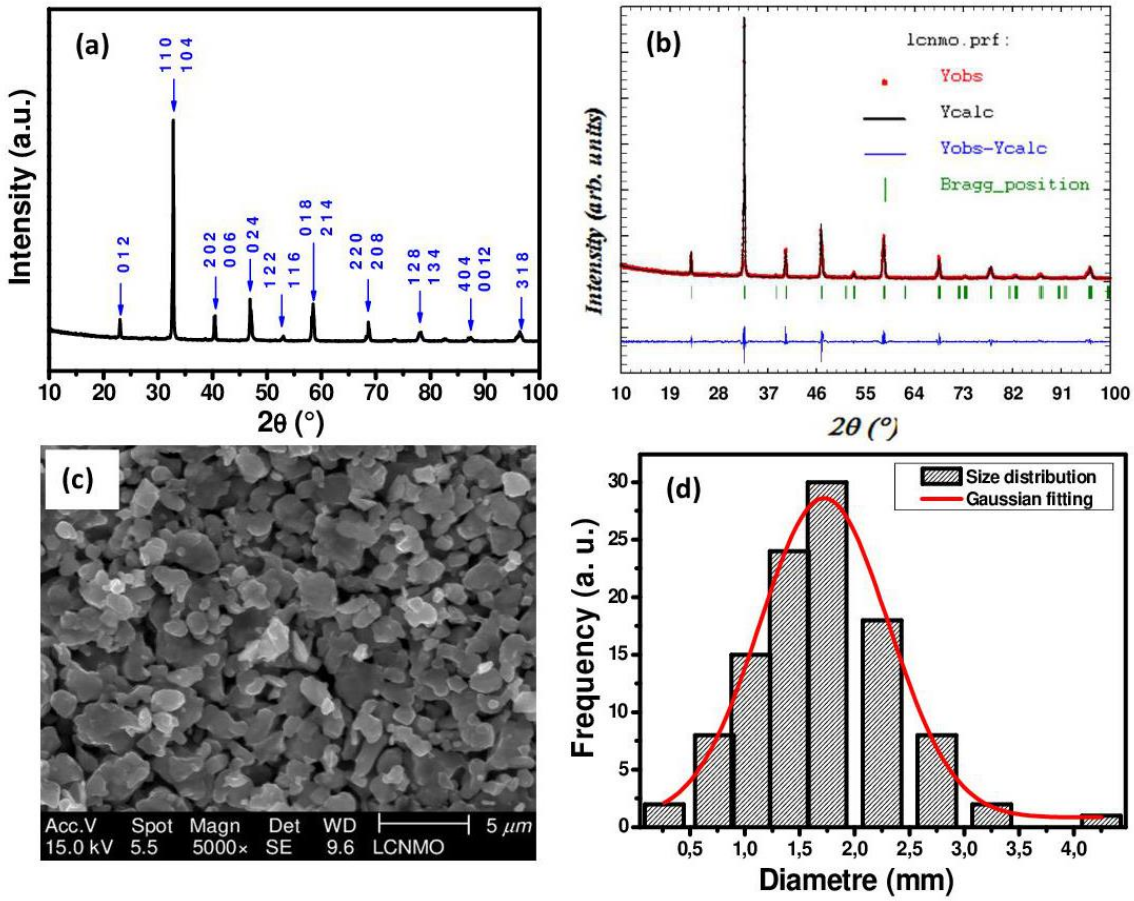

Fig. 2: (a) X-ray diffraction pattern for $La_{0.6}Ca_{0.2}Na_{0.2}MnO_3$ perovskite. **(b)** Rietveld analysis of XRD pattern. The bottom line (blue) represents the difference between the XRD data (red) and calculated fit (black), and the green lines are Bragg positions. All peaks of the perovskite phase are indexed in the hexagonal setting of the rhombohedral $R\bar{3}c$ symmetry. **(c)** SEM image. **(d)** Particle size distribution.

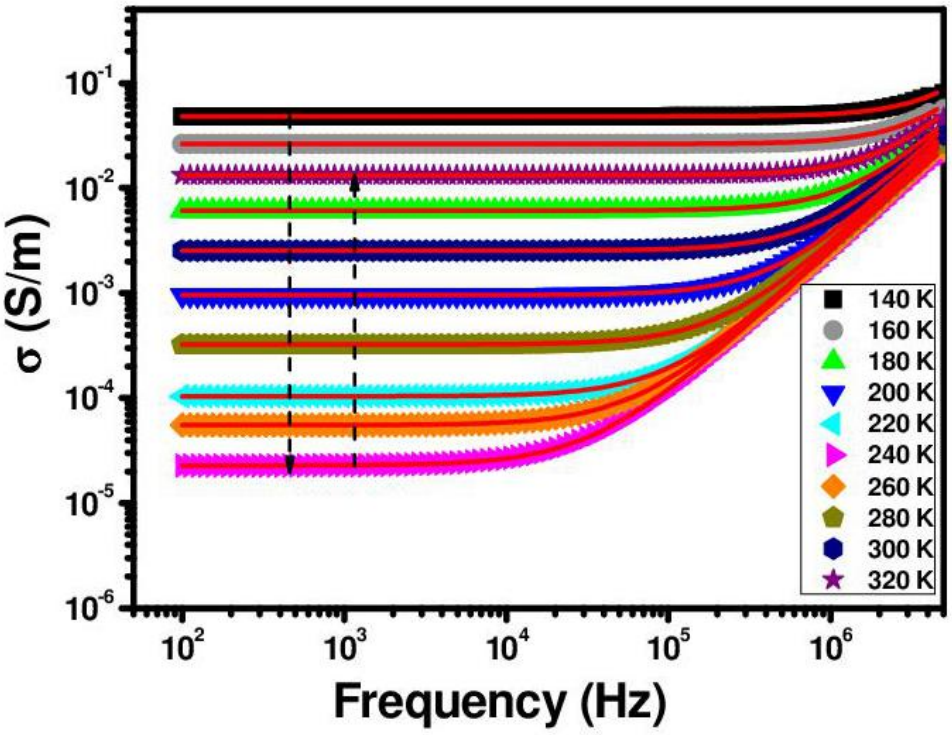

Fig. 3: Variation of conductivity as a function of frequency at different temperatures for $La_{0.6}Ca_{0.2}Na_{0.2}MnO_3$ perovskite. Red solid lines represent the fitting to the experimental data using the universal Jonscher power law.

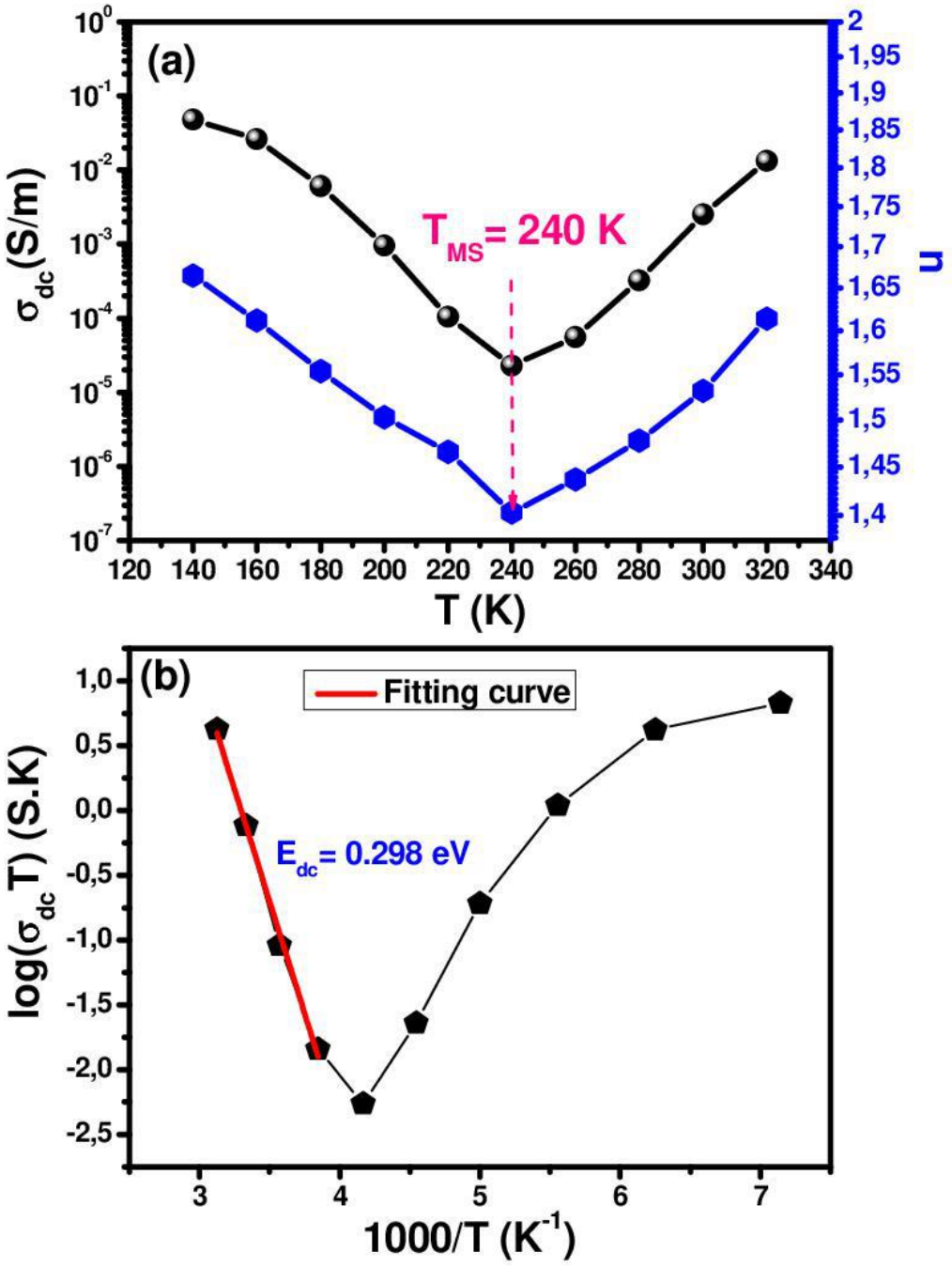

Fig. 4: (a) Variation of *dc* conductivity (σ_{dc}) and exponent (n) as a function of temperature for $La_{0.6}Ca_{0.2}Na_{0.2}MnO_3$ perovskite. **(b)** Variation of the $\log(\sigma_{dc}T)$ vs. (1000/T).

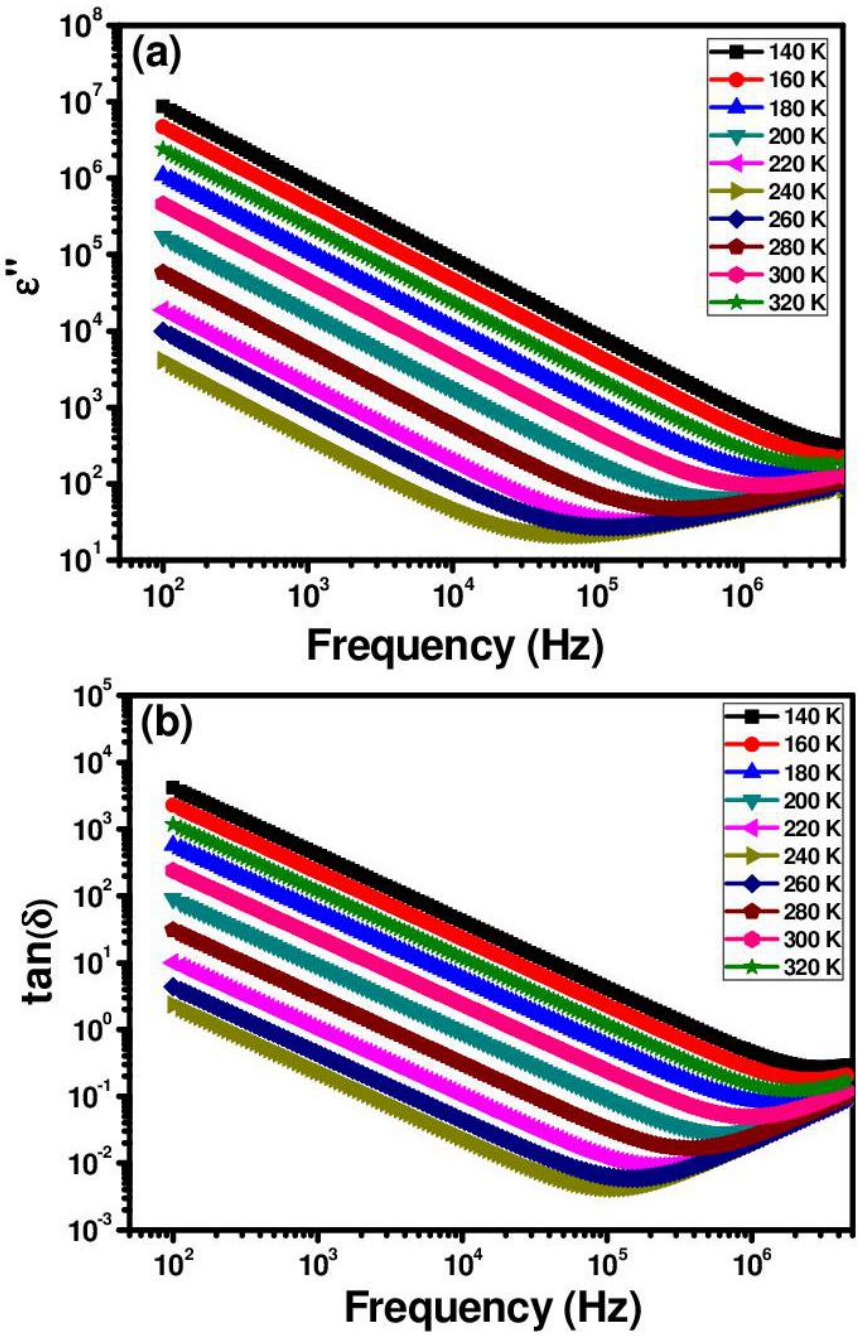

Fig. 5: Frequency dependence at different temperatures of **(a)** imaginary part of permittivity and **(b)** loss factor for $La_{0.6}Ca_{0.2}Na_{0.2}MnO_3$ perovskite.

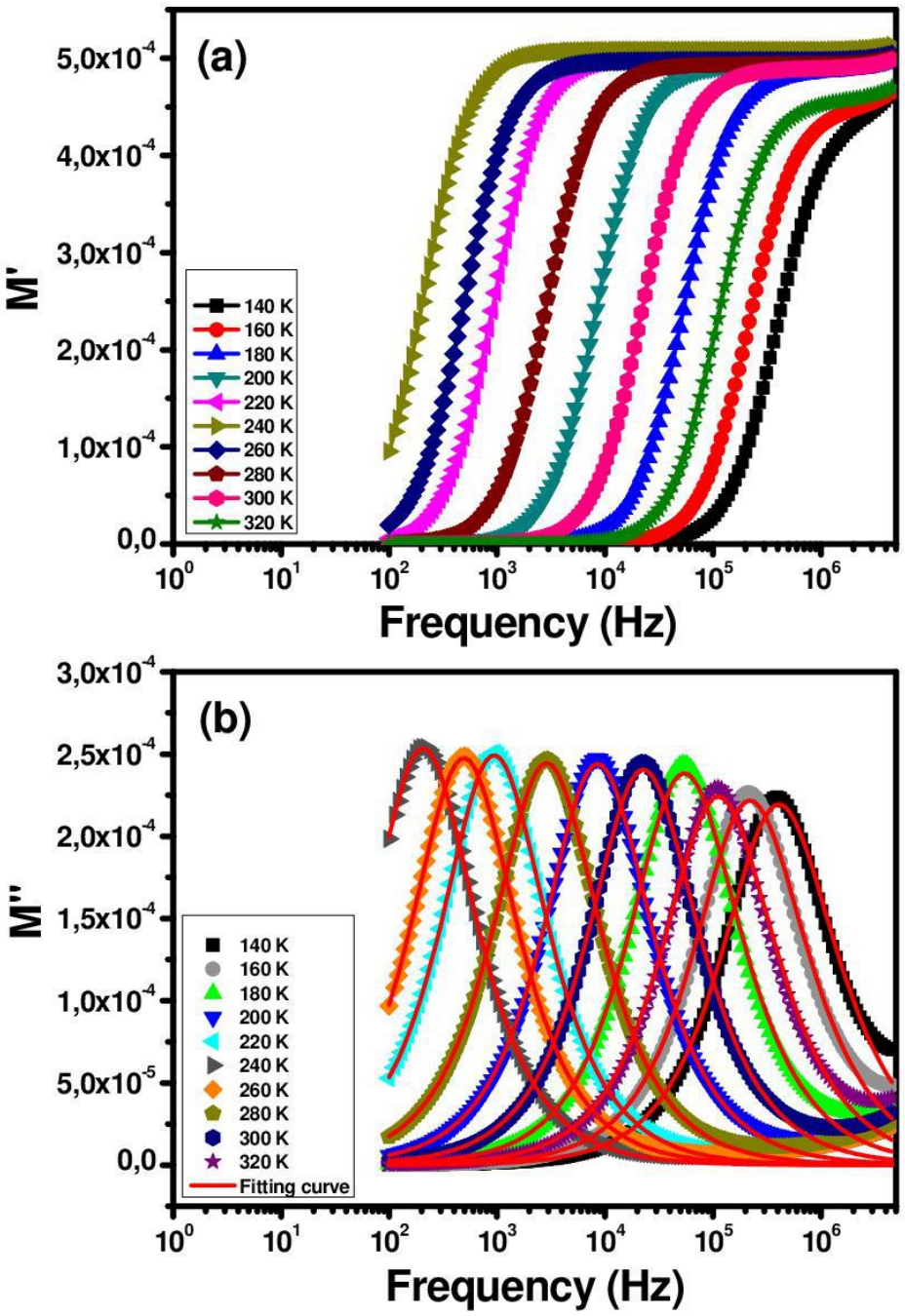

Fig. 6: Frequency dependence at different temperatures of **(a)** real part (*M'*) and **(b)** imaginary part (*M''*) of electrical modulus for $La_{0.6}Ca_{0.2}Na_{0.2}MnO_3$ perovskite. Red solid lines represent the fitting to the experimental data of *M''(f)* using KWW function.

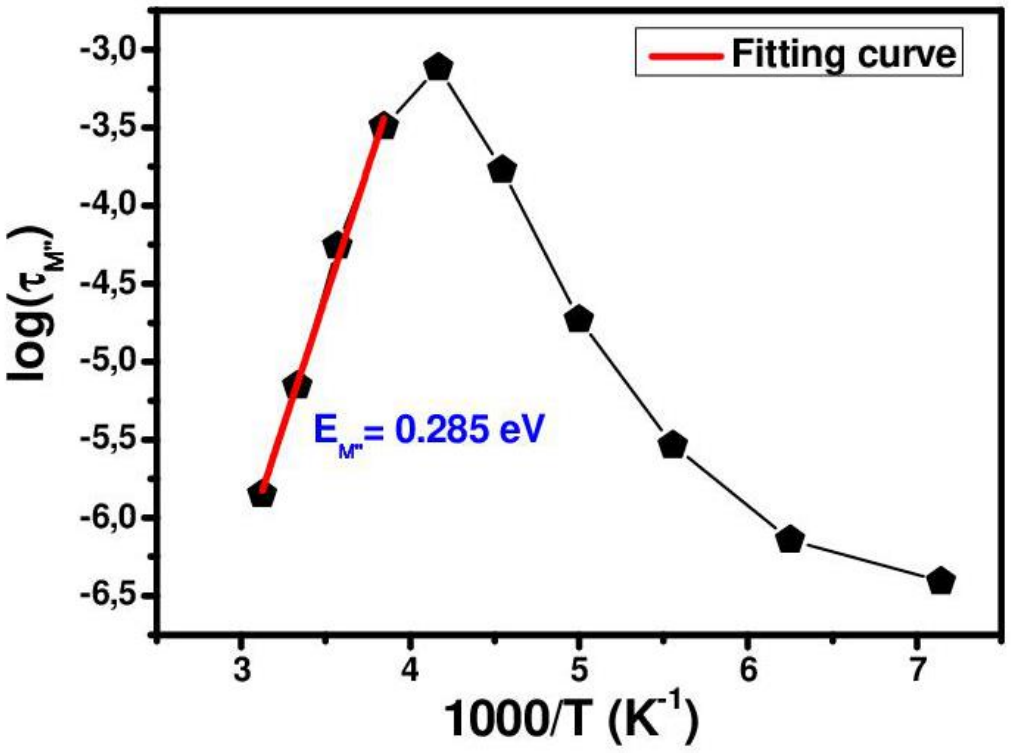

Fig. 7: Arrhenius plot of $Ln(\tau_{M''})$ vs. $(1000/T)$ for $La_{0.6}Ca_{0.2}Na_{0.2}MnO_3$ perovskite.

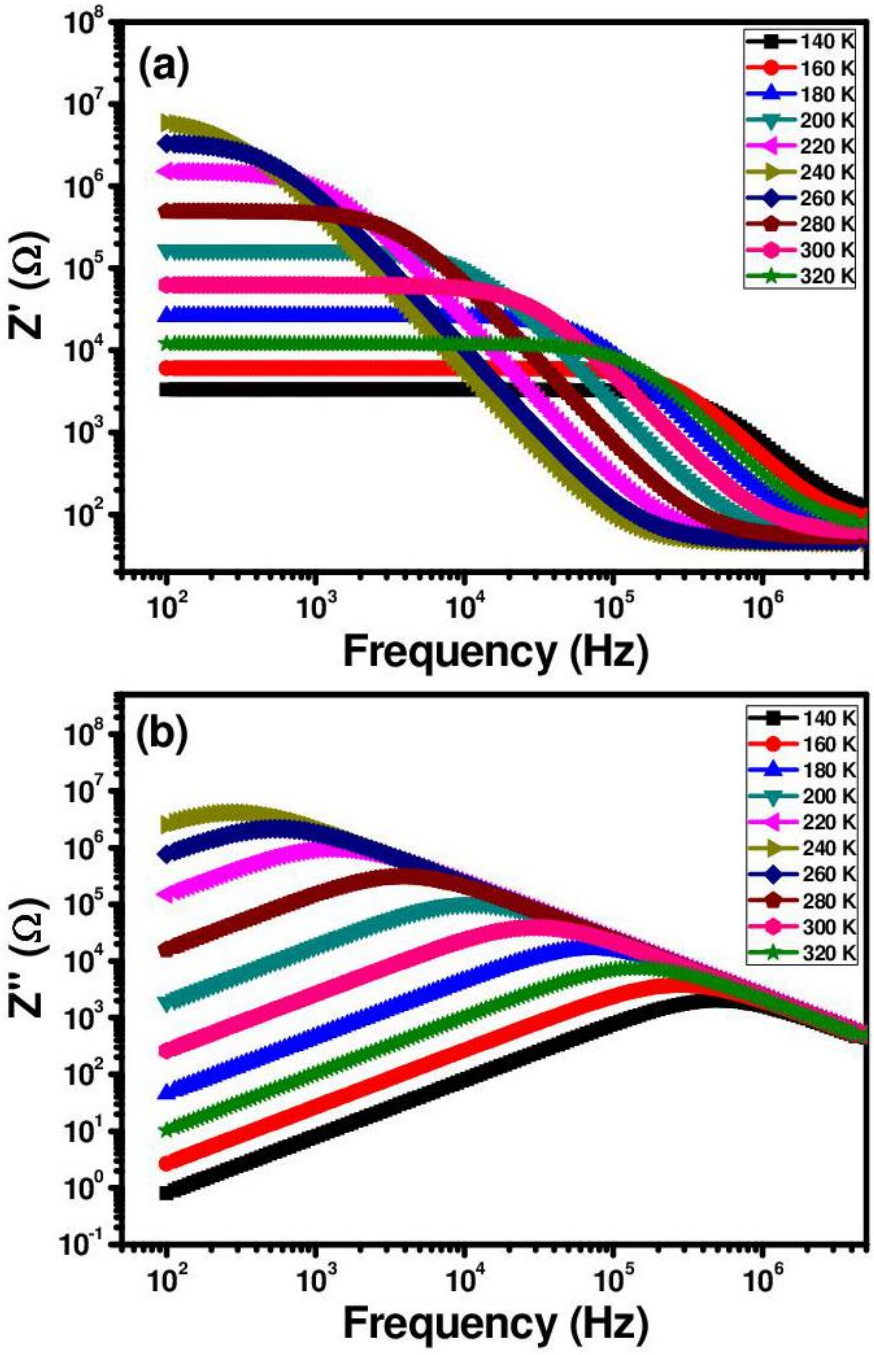

Fig. 8: Frequency dependence at different temperatures of: **(a)** real part *Z′* of impedance and **(b)** imaginary part *Z″* of impedance for $La_{0.6}Ca_{0.2}Na_{0.2}MnO_3$ perovskite.

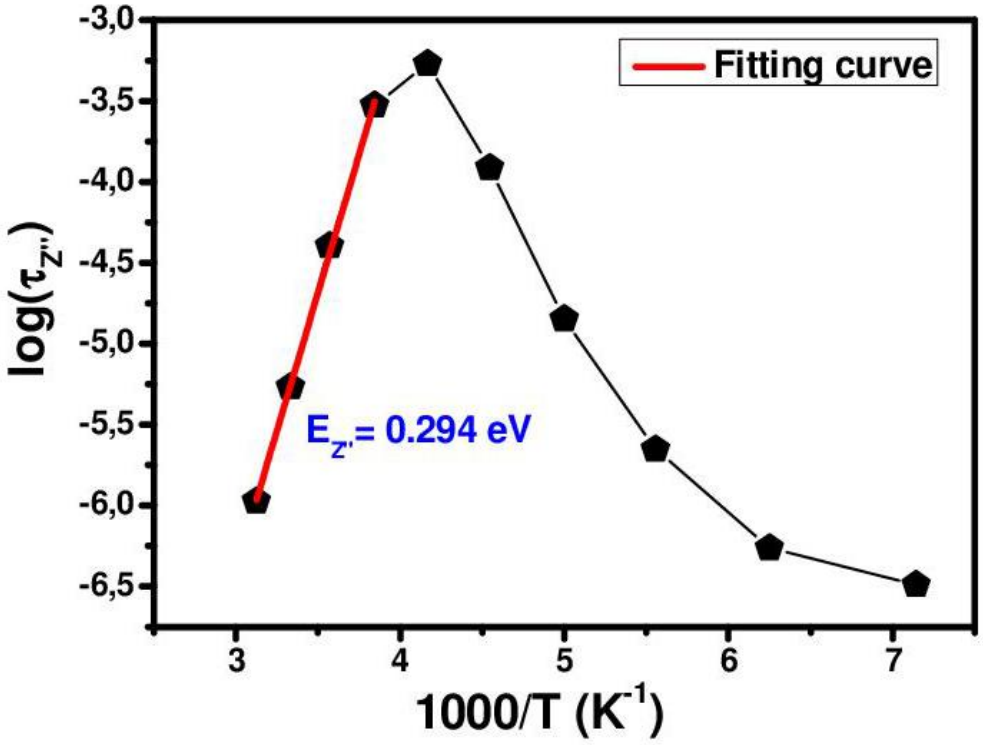

Fig. 9: Arrhenius plot of $Ln(\tau_{Z''})$ vs. $(1000/T)$ for $La_{0.6}Ca_{0.2}Na_{0.2}MnO_3$ perovskite.

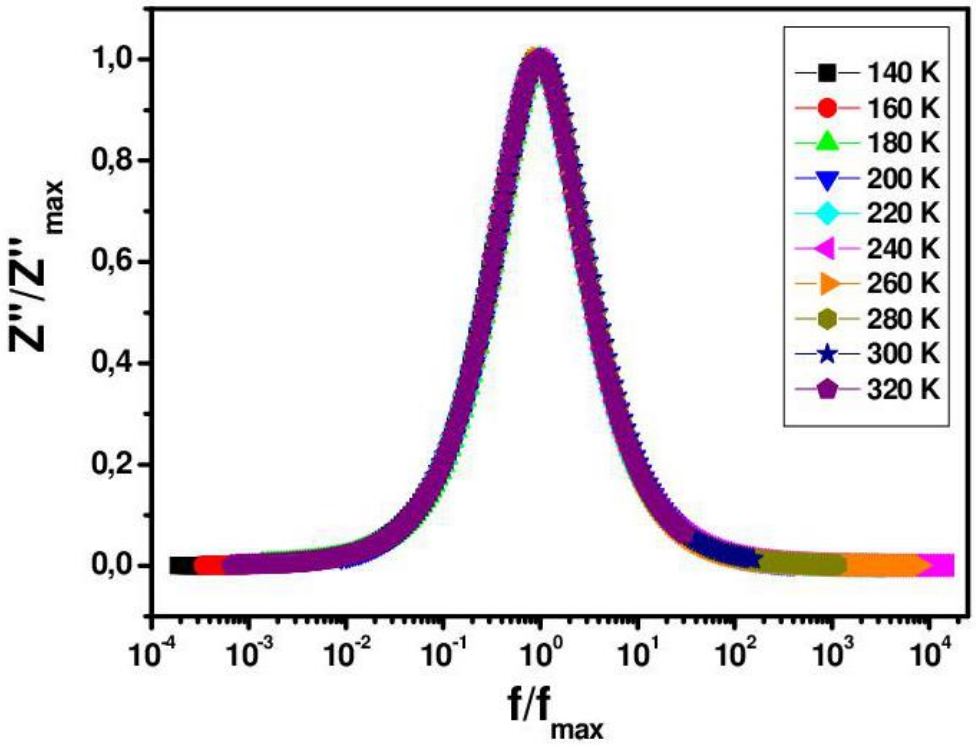

Fig. 10: Scaling behavior of the imaginary part of impedance (Z'') at various temperatures for $La_{0.6}Ca_{0.2}Na_{0.2}MnO_3$ manganite.

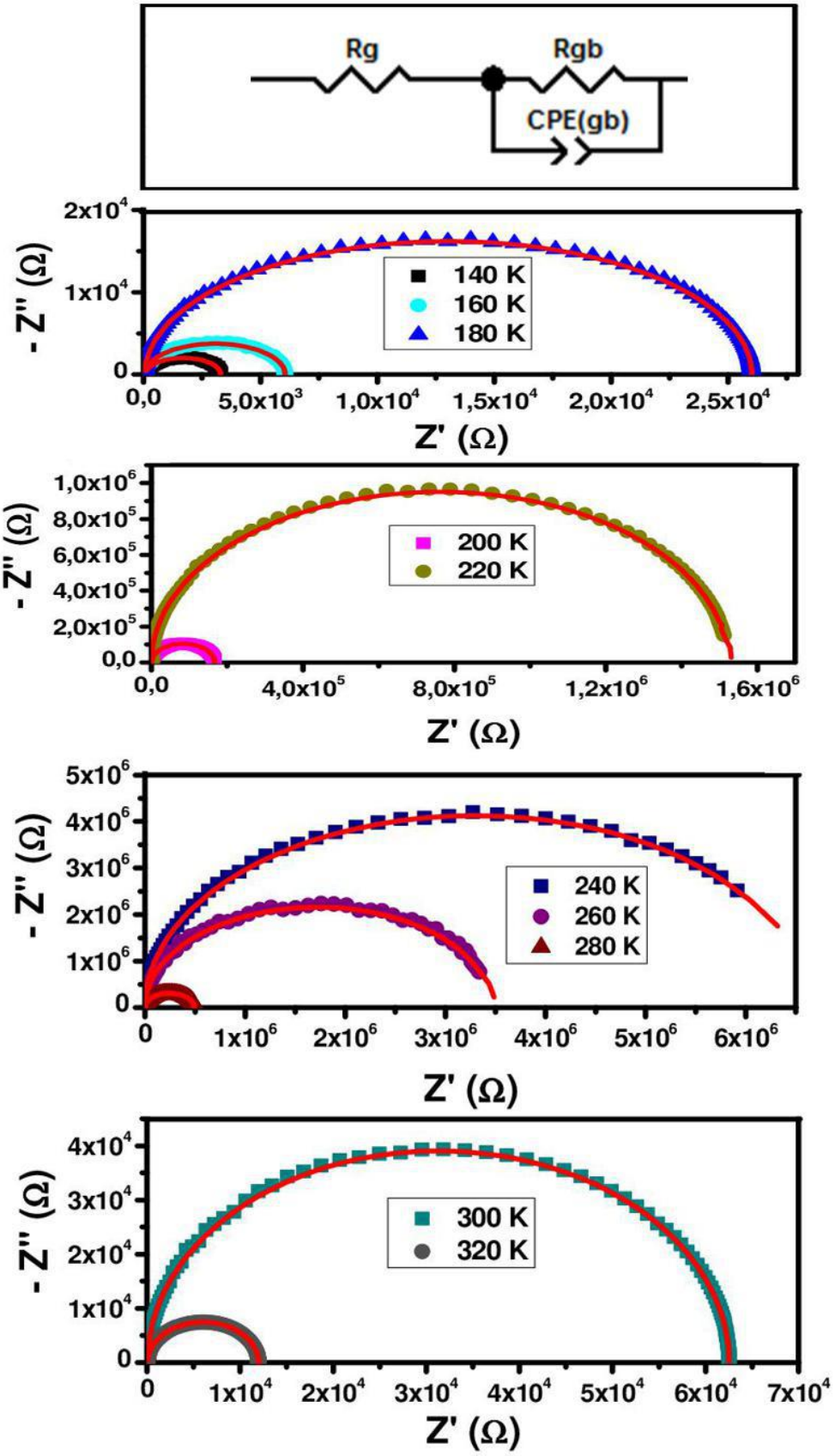

Fig. 11: Complex impedance spectra for $La_{0.6}Ca_{0.2}Na_{0.2}MnO_3$ perovskite at different temperatures fitting using *Zview* software with the appropriate equivalent electrical.

Table captions

Table 1: Fitting parameters obtained from the experimental data of imaginary part of modulus as a function of frequency at different temperatures for $La_{0.6}Ca_{0.2}Na_{0.2}MnO_3$ perovskite.

T(K)	$\boldsymbol{M''_{max} \times 10^{-4}}$	$\boldsymbol{\beta}$	f_{max}**(Hz)**	$\boldsymbol{\chi^2}$
140	2.194	0.905	407640	0.997
160	2.218	0.918	220540	0.996
180	2.384	0.927	54445	0.994
200	2.442	0.962	8537	0.989
220	2.494	0.984	940	0.991
240	2.535	0.985	207	0.992
260	2.477	0.986	494	0.991
280	2.447	0.975	2883	0.989
300	2.407	0.944	22619	0.989
320	2.241	0.918	112333	0.994

Table 2: Electrical parameters of equivalent circuit deduced from Nyquist plots at different temperatures for $La_{0.6}Ca_{0.2}Na_{0.2}MnO_3$ perovskite.

T(K)	***R_g (Ω)***	***R_{gb} (Ω)***	***$Q \times 10^{-11}$(F)***	***α***
140	105	3177	7.537	0.961
160	96	12579	7.214	0.979
180	87	51901	7.108	0.963
200	83	291859	6.711	0.979
220	76	1585801	6.314	0.986
240	71	2573047	6.125	0.973
260	86	660164	6.337	0.984
280	92	203108	6.591	0.986
300	102	91859	6.684	0.979
320	108	34529	6.762	0.975